NANO LETTERS

pubs.acs.org/NanoLett

DNA Tunneling Detector Embedded in a Nanopore

Aleksandar P. Ivanov,[†,||] Emanuele Instuli,[†,||] Catriona M. McGilvery,[‡] Geoff Baldwin,[§] David W. McComb,[‡] Tim Albrecht,[*,†] and Joshua B. Edel[*,†]

[†]Department of Chemistry, [‡]Department of Materials, and [§]Division of Molecular Biosciences, Imperial College London, Exhibition Road, London SW7 2AZ, U.K.

ABSTRACT We report on the fabrication and characterization of a DNA nanopore detector with integrated tunneling electrodes. Functional tunneling devices were identified by tunneling spectroscopy in different solvents and then used in proof-of-principle experiments demonstrating, for the first time, concurrent tunneling detection and ionic current detection of DNA molecules in a nanopore platform. This is an important step toward ultrafast DNA sequencing by tunneling.

KEYWORDS Nanopore sequencing, tunneling gap, DNA sequencing, label-free detection

Nanometer-scale pores (nanopores) are versatile single-molecule sensors for the label-free detection and structural analysis of biological polymers such as DNA, RNA, polypeptides, and DNA−protein complexes in solution.[1] In a typical nanopore experiment, biological molecules are electrokinetically driven through a nanopore by an externally applied electric field. This results in a characteristic blockade of the ionic current across the pore. From the ionic current blockade measurements, information on molecular properties such as length, composition, and interactions with other biomolecules can be extracted. When a biological polyelectrolyte such as DNA is driven through a pore with a diameter of a few nanometers, the molecule is unfolded from its coiled state and travels through the pore in a linear configuration. This gives rise to the unique opportunity to directly access the molecular structure of DNA. Unfortunately, the state-of-the-art detection based on ionic current blockade or fluorescence spectroscopy seems to lack the spatial and temporal resolution necessary to obtain structural information at the single base level.[2−4]

An alternative detection method based on tunneling transport in DNA (perpendicular to the DNA backbone) has recently been proposed to alleviate these limitations. Due to its quantum mechanical origin, the tunneling current decays rapidly with distance leading to enhanced spatial resolution and also provides molecular specificity. These characteristics form the basis of scanning tunneling microscopy (STM). Notably, identification of single (bio)molecules, nanoparticles, and even single nucleotides with tunneling currents has been predicted by theoretical work and shown experimentally by STM.[5−13]

Very recently, Tsutsui et al. were able to trap and identify single nucleotides between tunneling electrodes, providing the first experimental evidence toward a DNA sequencing-by-tunneling technology.[14] While exceptionally valuable as a proof of principle, these experiments were limited to single nucleotides[14] or performed in a STM environment.[7,8] A potentially much faster and hence more applicable approach is to fabricate a device that combines a nanopore with a tunneling junction. In such a configuration, the nanopore is used to "unfold" the DNA strand to a linear configuration, while a tunneling junction precisely aligned at the pore opening detects sequence-specific changes in the tunneling current. Unfortunately, while solid-state nanopores and nanogap tunneling electrodes are routinely fabricated on separate platforms, combining DNA translocation through a pore with concurrent tunneling and ionic current detection has yet to be realized.

Herein we present a simple but powerful approach to fabricate tunneling junctions aligned to a nanopore and perform proof-of-principle experiments demonstrating simultaneous detection of DNA translocations using both tunneling and ionic currents in a nanopore platform. It should be noted that there have been previous reports on the fabrication of nanopores[15,16] and nanofluidic devices[17−19] with integrated transverse electrodes; however, in all these cases the electrode gaps either were large or were not used for the detection of analyte. In our experiments we were able to fabricate electrode junctions with gap sizes sufficiently small to allow for tunneling transport to occur and precisely align the electrode junction to a nanopore for use in DNA translocation experiments.

The schematic of the final device is shown in Figure 1a. The experimental platform consists of a 5 mm × 5 mm silicon chip (300 μm thickness) with Si_3N_4 and Au layers (Figure 1a,b). Briefly, the fabrication process was as follows: Initially, Si_3N_4 was deposited by low pressure chemical vapor

* To whom correspondence should be addressed, t.albrecht@imperial.ac.uk and joshua.edel@imperial.ac.uk.

|| These authors contributed equally to this work.

Received for review: 11/3/2010
Published on Web: 12/06/2010

DOI: 10.1021/nl103873a | *Nano Lett.* **2011,** *11,* 279–285

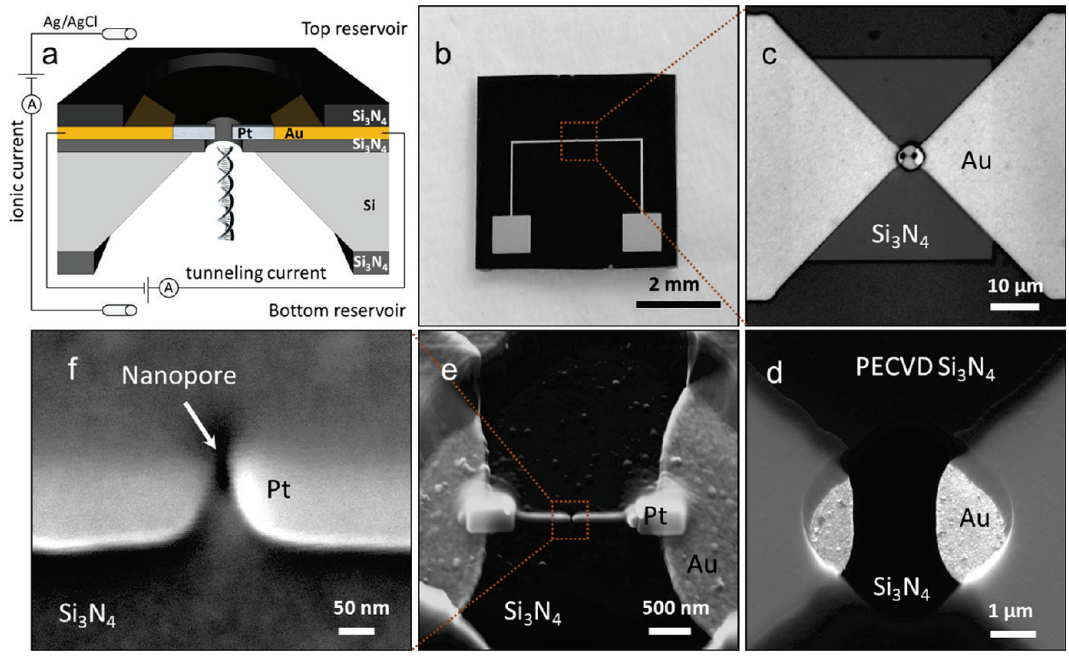

FIGURE 1. (a) Schematic of the nanopore/nanogap device integrated into an electrochemical cell. The tunneling junction is located at the exit of the nanopore. DNA is inserted in the bottom reservoir and electrophoretically driven through the nanopore and the tunneling junction. (b) Optical image of the 5 mm ×5 mm chip. (c) Free-standing 40 μm × 40 μm Si_3N_4 membrane aligned to the Au microelectrodes. (d) SEM image of the window in the PECVD Si_3N_4 layer opened by RIE. (e) SEM image of the Pt nanoelectrodes fabricated by EBID. The additional Pt contact pads (250 × 500 nm) were deposited to improve electrical connection to the Au microelectrodes. (f) Magnified SEM image showing the nanopore aligned to the Pt nanoelectrodes.

deposition (LPCVD) on both faces of a bare silicon ⟨100⟩ wafer to a thickness of 70 nm. Microelectrodes with a 2 μm gap (50 nm thick gold with 10 nm chromium adhesion layer, Figure 1b) were fabricated by conventional optical lithography on the front face of the wafer. An additional 300 nm thick layer of Si_3N_4 was deposited by plasma enhanced chemical vapor deposition (PECVD). Windows (5 μm × 5 μm) centered at the microelectrode tips were opened in the PECVD Si_3N_4 layer (Figure 1c,d). The additional Si_3N_4 layer reduces the membrane capacitance and Faradaic currents by minimizing the electroactive area. Furthermore, the additional Si_3N_4 layer helps to improve the mechanical strength of the membrane. A window in the LPCVD nitride on the back face of the wafer was opened by reactive ion etching (RIE), followed by wet etch of the silicon in KOH solution, resulting in a 70 nm thick free-standing Si_3N_4 membrane (40 μm × 40 μm) aligned to the microelectrodes (Figure 1c,d).

Fabrication of the nanopores and the electrode junctions was performed using a dual beam focused ion beam (FIB)/scanning electron microscope (SEM) instrument (Zeiss 1540XB). This allowed for the entire fabrication and alignment process to be controlled in situ and monitored in real time. Single pores were milled into the membrane and in between the two Au microelectrodes by FIB. Pores with diameters of 50−80 nm were milled in 2.5 s at a beam current of 1 pA. The pore milling process is similar to what has been previously described by our research groups.[20,21]

Once the pores were milled, the Pt nanoelectrodes were fabricated by electron beam induced deposition (EBID). In this process, the gaseous methylcyclopentadienyl(trimethyl)Pt precursor is directly injected in the SEM chamber and decomposed by the interaction of the electron beam with the surface.[22] In order to ensure a low material growth rate, the process was carried out at low precursor pressure (7×10^{-6} mbar, base pressure 2×10^{-6} mbar). Under these conditions we would expect the deposit to consist of nanometer-sized metal crystals embedded in an amorphous carbon matrix.[23] We determined the conductance of these wires to be 420 nS (vide infra), which is sufficient for the present application.

Finally, for the fabrication of the tunneling junctions, lateral broadening of the metal deposit has to be taken into account, which decreases the actual gap size compared to the nominal size as defined in the design template. Komuro et al. have reported the fabrication of tungsten-based tunneling junctions on plain SiO_2 using EBID and WF_6 as a precursor.[24] These authors observed electron tunneling for junctions with nominal gap sizes larger than 25 nm. However, due to the strong distance dependence of the tunneling effect, the actual gap size is expected to be on the range of 3 nm. In our experiments, electrode junctions deposited with a nominal gap size of 50−60 nm (exposure time 4 s at 30 kV) exhibited tunneling behavior. We further optimized the geometry of the nanogap by performing the deposition at an angle of 54° with respect to the electron beam. This

DOI: 10.1021/nl103873a | *Nano Lett.* **2011,** *11,* 279–285

allowed us to exploit the lateral broadening effect to decrease the nanowire width and height in the vicinity of the nanogap, Figure 1f.

We have fabricated 126 junctions with a nanopore. Inhomogeneity of the substrate surface, sample charging, and stage drift gave rise to an uncertainty in the localization of the nanogap relative to the nanopore in some devices (Figure S1, Supporting Information). The electrode gap was precisely aligned with the nanopore in 60% of the devices. Out of these, 20% exhibited tunneling characteristics that were stable and reproducible over several days. These devices were then used for DNA translocation experiments. For comparison, we also performed tunneling spectroscopy experiments on devices where the electrode gap was not aligned to the nanopore in order to verify that the presence of the pore does not affect the tunneling characteristics.

In a control experiment, we determined the (ionic) conductance of the device before and after Pt electrode deposition. If the electrode junction is precisely aligned with the nanopore and the gap size is smaller than the pore diameter, a significant decrease in the pore conductance would be expected. This is experimentally observed and shown in Figure 2 for a representative set of devices.

Figure 2a shows representative ion current vs bias voltage plots before (closed circles) and after electrode deposition (open circles), including SEM images of the respective device (insets). The pore conductance G, as determined from the slope of these traces, decreases from 71.6 ± 0.1 to 6.0 ± 0.1 nS. For the device before electrode deposition, G is in good agreement with the calculated value using eq 1 based on the geometrical dimensions of the pore (obtained from SEM imaging and the thickness of the membrane), which yields 52 ± 15 nS. The relatively large error of the latter emerges from the uncertainty in the pore diameter and membrane thickness.

$$G = \frac{\pi}{4}\frac{d_{\text{pore}}^2}{L_{\text{pore}}}\left((\mu_{\text{K}} + \mu_{\text{Cl}})n_{\text{KCl}}e + \mu_{\text{K}}\frac{4\sigma}{d_{\text{pore}}}\right) \quad (1)$$

d_{pore} is the (effective) pore diameter, L_{pore} the (effective) length of the pore, μ_{K} and μ_{Cl} are the electrophoretic mobilities of K^+ and Cl^-, respectively, n_{KCl} is the number density of the electrolyte, e the elementary charge, and σ is the surface charge density in the nanopore.[21,25]

Since eq 1 is strictly only valid for cylindrical pores with a high aspect ratio, it cannot provide reliable estimates of G for devices after electrode deposition due to the rather complex geometry. Rather, we use eq 1 and the experimentally determined value of G to estimate the effective pore diameter. Neglecting the surface contribution to G due to the high electrolyte concentrations used, we rearrange eq 1 and obtain

$$d_{\text{pore}} \approx \left(\frac{4GL_{\text{pore}}}{\pi(\mu_{\text{K}} + \mu_{\text{Cl}})n_{\text{KCl}}e}\right)^{1/2} \quad (2)$$

A comparison of the calculated effective pore diameter determined using eq 2 is shown in Figure 2b for a total of 10 representative devices. Devices 1−5 do not have Pt nanogaps. The calculated pore diameters range from 50 to 80 nm (green circles) and compare well with values obtained by SEM imaging (black squares). A further set of devices (6−10) with Pt nanogaps exhibits significantly reduced pore diameters typically well below 10 nm (5−18 nm). Qualitatively, these values are in line with what was observed in SEM images.

After electrode deposition, the next step in the fabrication process was to ascertain that the tunneling junction is functional. To this end, we performed $I-V$ tunneling spectroscopy in a range of different solvents with different

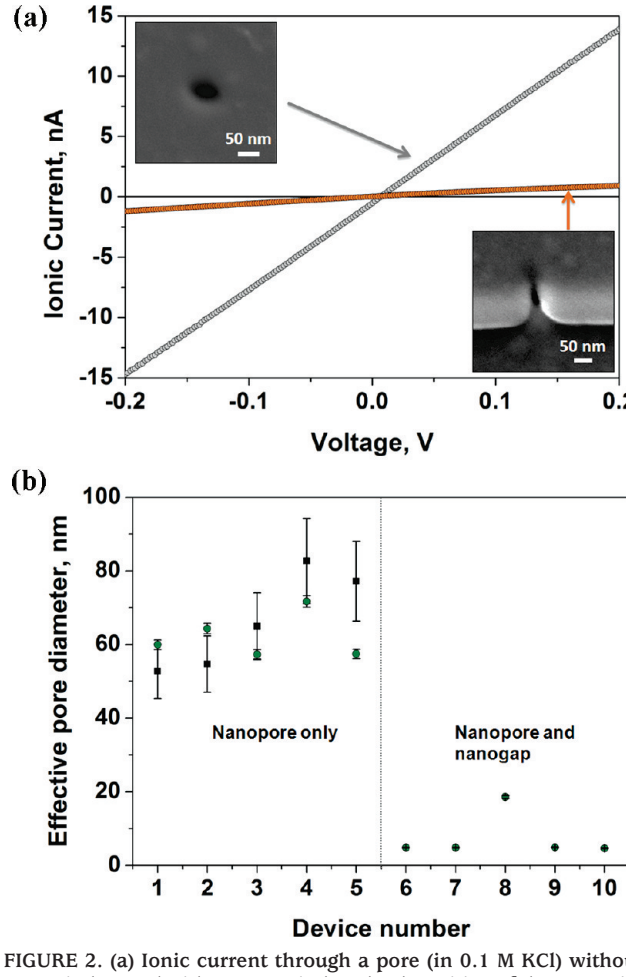

FIGURE 2. (a) Ionic current through a pore (in 0.1 M KCl) without (gray circles) and with (orange circles) the deposition of the nanowire electrodes: top left inset, SEM image of a pore drilled by FIB; bottom right inset, SEM image of an aligned nanopore/nanogap architecture. (b) Effective pore diameter for 10 typical devices before (1−5) and after (6−10) nanoelectrode fabrication as calculated from ionic current conductance (green circles) and SEM data (black squares).

DOI: 10.1021/nl103873a | Nano Lett. 2011, 11, 279–285

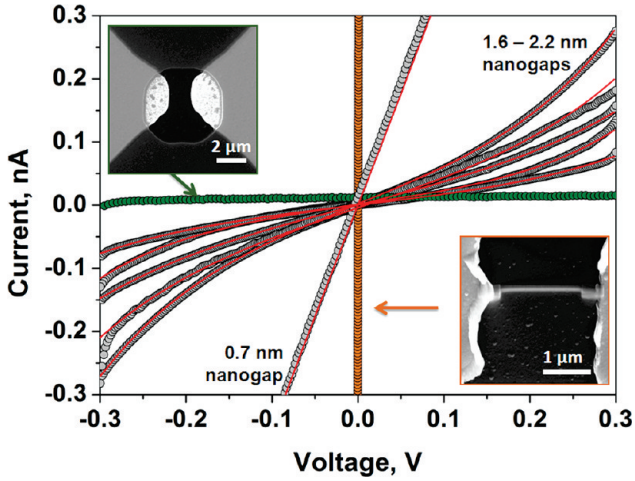

FIGURE 3. Nanogap tunneling spectroscopy in 0.1 M $NaClO_4$ at room temperature (297 K) and corresponding fits (red dotted line). The $I-V$ curves for a nanogap with a smaller gap size (0.7 nm) and for controls 1 (green) and 2 (orange) are also shown for comparison. SEM images of the controls are shown as insets.

tunneling barriers (air, 0.1 M $NaClO_4$, *n*-hexane and dimethyl sulfoxide (DMSO)). The resulting $I-V$ spectra were fit according to the Simmons model, which is a standard model to describe tunneling under a potential barrier.[9,26] Moreover, we use the low-bias limit implying that the tunneling bias V_{bias} is small compared to the tunneling barrier height Φ_B. This is a reasonable approximation since the Φ_B for water-filled junctions has been reported to be on the order of 1 eV whereas we applied a bias between ±0.3 V. For each junction, multiple $I-V$ curves were recorded at a scan rate of 0.02 V/s.

$$I = A\left(\frac{e}{4\pi^2\hbar d^2}\right)\left\{\left\{\left(\Phi_B - \frac{eV}{2}\right)\exp\left[-\frac{2(2m)^{1/2}}{\hbar}\left(\Phi_B - \frac{eV}{2}\right)^{1/2}d\right] - \left(\Phi_B + \frac{eV}{2}\right)\exp\left[-\frac{2(2m)^{1/2}}{\hbar}\left(\Phi_B + \frac{eV}{2}\right)^{1/2}d\right]\right\} + B \quad (3)$$

d is the gap distance, A the active tunneling area, and B is a parameter that takes into account any current offset at zero bias (due to residual Faradaic processes or minor calibration errors).

At first, we compare different devices (with different gap sizes) in the same medium (i.e., constant barrier height). Figure 3 shows $I-V$ curves in 0.1 M $NaClO_4$ for six typical Pt nanogap devices and two controls: a device with Au microelectrodes separated by a 2 μm gap (control 1) and one with a single Pt nanowire bridging both Au microelectrodes (same deposition conditions as the gaps, control 2). The $I-V$ curves for the Pt nanogap devices are nonlinear (in accordance with eq 3) with current levels significantly higher than in control 1 (0.01 nS) and lower than in control 2 (420 nS). For tunneling junctions deposited with nominal gaps sizes between 50 and 60 nm, we measured tunneling conductance in the range of 0.2–4 nS.

We fit the $I-V$ curves according to eq 3 in order to extract the electrode gap size and tunneling barrier. For 0.1 M $NaClO_4$, these parameters were determined to be between 1.6 and 2.2 nm and 0.69 ± 0.27 eV, respectively. Importantly, the barrier height was in good agreement with previously reported values obtained by electrochemical STM.[27] Additionally, the measured tunneling currents and the corresponding calculated gap distances compare well with results previously reported for tunneling gaps fabricated with variable gap distance.[14]

Previously, nonlinear $I-V$ curves have been reported for Pt nanowires fabricated by EBID and rationalized by electron tunneling between Pt crystallites.[28] In order to discriminate from this case and to confirm that we have fabricated functional tunneling junctions, we performed $I-V$ spectroscopy for the tunneling junctions in different solvents (i.e., with different barrier heights).

Tunneling barriers for hexane, DMSO, and water have been reported to be 3.46, 2.12, and 0.93 eV respectively.[29] The barrier height for air has been reported to range from 0.7 to 4.7 eV depending on the local environment.[29–31] According to eq 3 such variations translate into significant differences in the tunneling current. On the other hand, in the case of a single nanowire, the measured current is expected to show little variation with the solvent, since its conductivity is dominated by the nanowire material.

For devices fabricated with a nanogap (Figure 4a–c), we observed significant, but reproducible variation in the $I-V$ curves, depending on the solvent used. It should be noted that we randomized the sequence of solvents, in order to exclude any interference from cross-contamination. Effective barrier heights were calculated to be 0.69 ± 0.27 eV for 0.1 M $NaClO_4$, 2.07 ± 0.64 eV in DMSO, and 3.32 ± 0.78 eV in *n*-hexane. All these values are in good agreement with the literature (see above).[29] In air, we observed a relatively low barrier height of 1.35 ± 0.52 eV, which is likely due to vapor condensation in the gap. These results are comparable to those obtained by Hahn et al.[31] For control 2 (Pt nanowire, no gap), under the same experimental conditions, solvent dependence was not observed (Figure 4d), which confirms that we can distinguish functional tunneling junctions from short-circuited and other dysfunctional devices.

Fully characterized devices exhibiting tunneling behavior were then used to perform DNA translocation experiments. Simultaneous measurement of tunneling and ionic currents was carried out by combining a Gamry Reference 600 potentiostat (tunneling current measurements, 5 kHz acquisition frequency, no filter) and an Axopatch 200B patch-clamp amplifier (ionic current measurements, 50 kHz acquisition, 5 kHz Bessel filter). The nanopore/nanogap device was packaged in a glass flow cell with two reservoirs filled with 1 M KCl, 10 mM Tris-HCl, 1 mM EDTA. Ag/AgCl electrodes were inserted in each reservoir and connected to the Axopatch amplifier. The Ag/AgCl electrode in the top reservoir was used as common ground for both the Axo-

DOI: 10.1021/nl103873a | *Nano Lett.* **2011,** *11,* 279–285

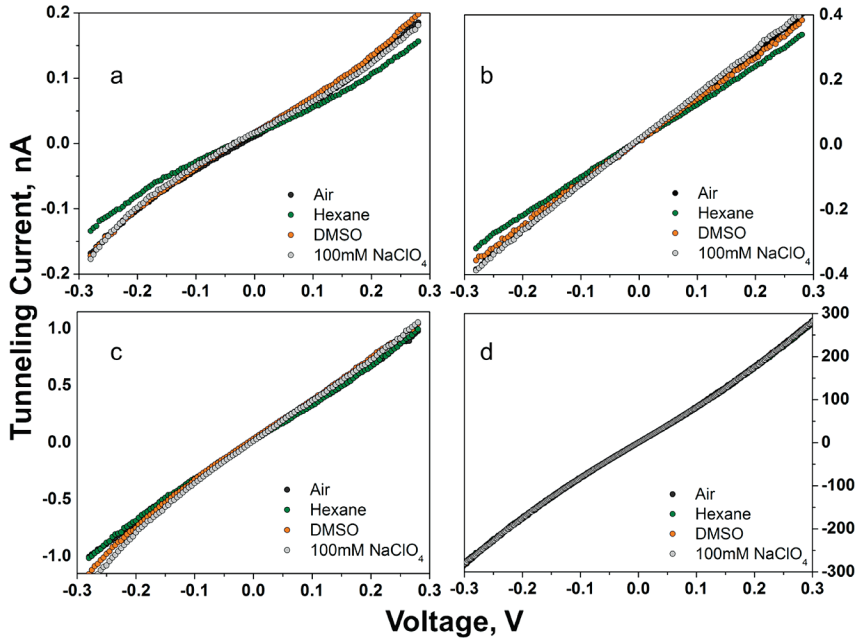

FIGURE 4. Tunneling spectroscopy performed in air (black), *n*-hexane (green), DMSO (orange), and 0.1 M $NaClO_4$ (gray) for three different devices with a nanogap (a−c) and a single nanowire (d).

patch and Gamry instruments. λ-DNA (48.5 kbp, 10 μg/mL) was added to the bottom reservoir (opposite to the tunneling gap, as shown in Figure 1a) in order to minimize spontaneous adsorption of DNA molecules to the electrode gap. In this configuration, the DNA must translocate through the pore in order to reach the tunneling junction. For translocation experiments, a bias voltage, $E_i = -0.8$ V, was applied to the Ag/AgCl electrodes. The bias voltage across the tunneling junction was set to $E_t = 0.3$ V.

Typical ion current−time (black) and tunneling current−time (red) traces are shown in Figure 5. We have performed statistical analysis on a total of 3429 events (cf. Figure S2 in the Supporting Information) and observed two classes of events: short-lived transients (type I) and longer lived events (type II). Type I events exhibited a mean dwell time τ of 0.3 ± 0.2 ms and a mean amplitude of 2.5 ± 0.7 nA. They formed the majority of the observed events; a typical section of the ion current−time trace is shown in Figure 5a. With the extended length of λ-DNA being 16.5 μm, this translates into a translocation speed of 5.5 cm/s. Importantly this is in excellent agreement with previous results by Chen et al. They reported translocation speeds between approximately 2 and 6 cm/s, depending on the bias voltage at a membrane thickness of ∼10 nm.[32]

For a proper quantitative comparison, the respective values should be corrected for the actual electric driving field. However, with the geometry of our electrode/nanopore device being rather complex, we can only estimate its magnitude. Taking the nominal thickness of the Si_3N_4 membrane of 70 nm as a reference, we obtain a value of 0.8 V/70 $\times 10^{-9}$ m = 1.1 $\times 10^7$ V/m, which is somewhat smaller than the values given by Chen et al. (ca. 2 $\times 10^7$ to 6 $\times 10^7$ V/m).[32]

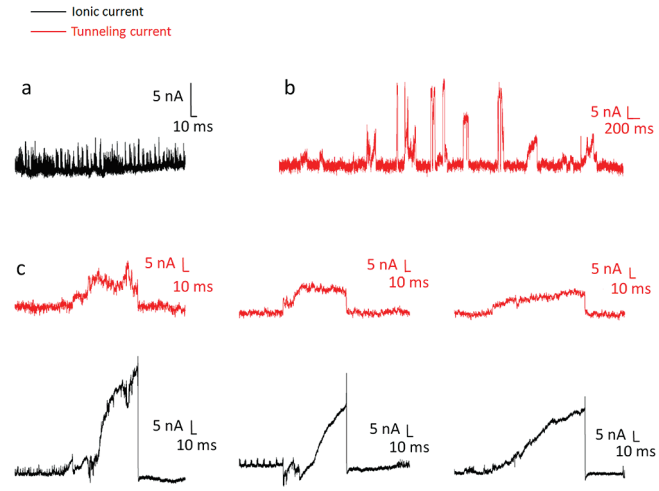

FIGURE 5. λ-DNA events detected with the electrodes/nanopore architecture in an electrolyte solution of 1 M KCl, Tris-HCl EDTA buffer, $E_t = 0.3$ V and $E_i = -0.8$ V. Note that ionic current (black curves) is always negative and that events occurring upward decrease the nanopore conductance. Acquisition frequency: 50 kHz for ionic current, 5 kHz Bessel filter; 5 kHz for tunneling, no filter. (a) Ionic current for short-lived type I events. (b) Tunneling current for long-lived type II events. (c) Examples of coincident type II events detected in both detection channels.

Since the tunneling junction represents a significant constriction in the pore (and thus a source of resistance), the effective membrane thickness is likely to be smaller than 70 nm, resulting in a larger local electric field. On the basis of the translocation speed observed in our experiments and comparison with previously reported data, we are confident that the type I events are actually DNA translocation events. "Bumping events", i.e., ion current blockades that originate from DNA colliding with the pore entrance without actually

DOI: 10.1021/nl103873a | *Nano Lett.* **2011,** *11,* 279–285

entering the pore, are expected to be even faster than the type I events and were not detected in our experiments.

It should also be stated that these events were not detected when measuring the tunneling current. This could have several reasons: First, the tunneling data are recorded at a rate of 5 kHz (200 μs); therefore, the short-lived type I events are most likely too fast to be recorded. Unfortunately, in the present configuration faster acquisition rates were not possible. In further studies, we intend to modify the electronics to perform tunneling experiments at the same acquisition rate as that of the ionic current (50 kHz). Second, tunneling current modulation could be too small to be detected in the current experimental configuration. Previous work by Chang et al. and Tsutsui et al. showed tunneling current modulation due to individual bases of $\sim$10 pA.[8,14] If these values are also representative for tunneling current modulations for a DNA strand in the present configuration, such small variations are most likely embedded in the tunneling current noise, which is currently on the order of 1 nA; cf. Figure 5. Finally, since the tunneling-active area is smaller than the cross-sectional area of the pore, there is a nonzero probability that DNA strands actually bypass the tunneling junction. The ratio of bypassing DNA and DNA detected by the tunneling junction depends on the device design and can, in principle, be optimized. Interestingly, bypassing DNA would experience a larger constriction and translocate much faster than DNA going through the much narrower tunneling junction. In the latter, the DNA is also more likely to undergo structural changes, such as (partial) unzipping, to temporarily clog the pore and/or adsorb to the metal surface.

In accordance with this picture, we also observed longer-liver events (type II) with characteristic dwell times between 1.5 and 200 ms (Figure 5b). These events were recorded in both the tunneling and ionic current data. A total of 108 type II translocation events were detected. The mean dwell time and amplitude of the tunneling events were 4.7 $\pm$ 4.3 ms and 3.7 $\pm$ 0.4 nA, respectively. The increase in the tunneling current upon DNA translocation is in accordance with STM imaging data of DNA. The signals obtained in our experiments were higher, which could be due to the DNA/electrode coupling being stronger (stronger electronic overlap or multiple bases conducting in parallel). The dwell times for type II events were on average 16 times longer than for type I events. Tsutsui et al.[14] made similar observations stating that nonspecific binding between the DNA and the nanoelectrodes could be used to explain the spread over time. This is likely the case in our experiments and would explain the wide dwell time distribution.

Importantly the dwell time for the tunneling current compares well with that detected for the ionic current (Figure 5c). The ionic current had a mean dwell time τ of 6.3 $\pm$ 3.2 ms and mean amplitude of 7.0 $\pm$ 1.8 nA. The lower translocations times observed with the tunneling data are due to the DNA leaving the tunneling junction prior to the pore being fully unblocked. Furthermore, a small fraction of the type II events (20%) had a signal in either of the ionic current or tunneling traces, which is likely due to adsorption or bumping of the DNA on the electrode without any translocations taking place.

Conclusions. We have successfully developed a protocol for the fabrication of a solid state nanopore aligned to a tunneling junction using FIB milling and EBID. The devices were characterized and tested by measuring both ionic and tunneling currents in different solvents. Furthermore, proof-of-principle experiments were performed using λ-DNA as a test sample and we were successful in detecting DNA translocation events simultaneously in both the ionic and tunneling currents. Two types of translocation events were recorded: first, type I events occurred on a submillisecond time scale and were recorded only in the ionic current channel. These events were not detected in the tunneling current. Second, type II events consisted of translocations greater than 1 ms in duration and were recorded in both the ionic current and tunneling current channels. The longer translocation time when compared to type I is likely due to either adsorption or trapping in the tunneling junction. While the present study primarily focused on device fabrication and characterization, future studies will address details of the DNA translocation/detection process. These include (a) the optimization of acquisition frequencies, (b) surface modification to minimize DNA adsorption to the electrodes, and (c) the use of different DNA samples to study the effect of DNA structure and length, with a view on applications in DNA fragment sizing and sequence analysis. The new technology described in this paper opens up the door for high-throughput tunneling-based analysis of DNA and other (bio)molecules in nanopores.

Acknowledgment. This work is supported by the Wellcome Trust. A.P.I. acknowledges the financial support by the Corrigan Foundation. The authors thank the London Centre for Nanotechnology and University of Minnesota Nanofabrication Center for some support in the nanofabrication procedures. We thank Jongin Hong, Guillaume Chansin, and Mariam Ayub for useful discussions and advice.

Supporting Information Available. Figures showing a TEM image of Pt nanogap, the nanopore nanogap offset, ionic current DNA data, and tunneling current DNA data. This material is available free of charge via the Internet at http://pubs.acs.org.

REFERENCES AND NOTES

(1) Dekker, C. *Nat. Nanotechnol.* **2007**, *2*, 209.
(2) Branton, D.; Deamer, D. W.; Marziali, A.; Bayley, H.; Benner, S. A.; Butler, T.; Di Ventra, M.; Garaj, S.; Hibbs, A.; Huang, X. H.; Jovanovich, S. B.; Krstic, P. S.; Lindsay, S.; Ling, X. S. S.; Mastrangelo, C. H.; Meller, A.; Oliver, J. S.; Pershin, Y. V.; Ramsey, J. M.; Riehn, R.; Soni, G. V.; Tabard-Cossa, V.; Wanunu, M.; Wiggin, M.; Schloss, J. A. *Nat. Biotechnol.* **2008**, *26*, 1146.
(3) Hong, J.; Lee, Y.; Chansin, C. A. T.; Edel, J. B.; deMello, A. J. *Nanotechnology* **2008**, *19*, 165205.
(4) Chansin, C. A. T.; Mulero, R.; Hong, J.; Kim, M. J.; deMello, A. J.; Edel, J. B. *Nano Lett.* **2007**, *7*, 2901–06.
(5) Zwolak, M.; Di Ventra, M. *Nano Lett.* **2005**, *5*, 421.

DOI: 10.1021/nl103873a | *Nano Lett.* **2011,** *11,* 279–285

(6) Lagerqvist, J.; Zwolak, M.; Di Ventra, M. *Nano Lett.* **2006**, *6*, 779.
(7) He, J.; Lin, L.; Zhang, P.; Lindsay, S. *Nano Lett.* **2007**, *7*, 3854.
(8) Chang, S.; Huang, S.; He, J.; Liang, F.; Zhang, P.; Li, S.; Chen, X.; Sankey, O.; Lindsay, S. *Nano Lett.* **2010**, *10*, 1070.
(9) Wang, W.; Lee, T.; Reed, M. A. Electrical Characterization of Self-Assembled Monolayers In *Nano and Molecular Electronics Handbook*; Lyshevski, S. E., Ed.; CRC Press: Boca Raton, FL, 2007; Chapter 1, p 3.
(10) Zhang, J.; Kuznetsov, A. M.; Medvedev, I. G.; Chi, Q.; Albrecht, T.; Jensen, P. S.; Mertens, S. F. L.; Ulstrup, J. *J. Am. Chem. Soc.* **2007**, *129*, 9162–9167.
(11) Haiss, W.; Albrecht[§], T.; van Zalinge, H.; Higgins, S. L.; Bethell, D.; Höbenreich, H.; Schiffrin, D. J.; Nichols, R. J.; Kuznetsov, Am. M.; Zhang, J.; Chi, Q.; Ulstrup, J. *J. Phys. Chem. B* **2007**, *111*, 6703–6712.
(12) Albrecht, T.; Guckian, A.; Kuznetsov, A. M.; Vos, J. G.; Ulstrup, J. *J. Am. Chem. Soc.* **2006**, *128*, 17132–17138.
(13) Albrecht, T.; Guckian, A.; Ulstrup, J.; Vos, J. G. *Nano Lett.* **2005**, *5*, 1451–1455.
(14) Tsutsui, M.; Taniguchi, M.; Yokota, K.; Kawai, T. *Nat. Nanotechnol.* **2010**, *5*, 286.
(15) Fischbein, M. D.; Drndic, M. *Nano Lett.* **2007**, *7*, 1329.
(16) Gierhart, B. C.; Flowitt, D. G.; Chen, S. J.; Zhu, Z.; Kotecki, D. E.; Smith, R. L.; Collins, S. D. *Sens. Actuators, B* **2008**, *132*, 593.
(17) Liang, X.; Chou, S. Y. *Nano Lett.* **2008**, *8*, 1472.
(18) Maleki, T.; Mohammadi, S.; Ziaie, B. *Nanotechnology* **2009**, *20*, 10.
(19) Tsutsui, M.; Taniguchi, M.; Kawai, T. *Nano Lett.* **2009**, *9*, 1659.
(20) Ayub, M.; Ivanov, A.; Hong, J.; Kuhn, P.; Instuli, E.; Edel, J. B.; Albrecht, T. *J. Phys.: Condens. Matter* **2010**, *22*, 454128.
(21) Ayub, M.; Ivanov, A.; Instuli, E.; Cecchini, M.; Chansin, G.; McGilvery, C.; Hong, J.; Baldwin, G.; McComb, D.; Edel, J. B.; Albrecht, T. *Electrochim. Acta* **2010**, *55*, 8237–8243.
(22) Utke, I.; Hoffmann, P.; Melngailis, J. *J. Vac. Sci. Technol., B* **2008**, *26*, 1197.
(23) Rotkina, L.; Oh, S.; Eckstein, J. N.; Rotkin, S. V. *Phys. Rev. B* **2005**, *72*, 233407.
(24) Komuro, M.; Hiroshima, H. *J. Vac. Sci. Technol., B* **1997**, *15*, 2809–2815.
(25) Smeets, R. M. M.; Keyser, U. F.; Krapf, D.; Wu, M. Y.; Dekker, N. H.; Dekker, C. *Nano Lett.* **2006**, *6*, 89.
(26) Simmons, J. G. *J. Appl. Phys.* **1963**, *34*, 1793.
(27) Albrecht, T.; Moth-Poulsen, K.; Christensen, J. B.; Guckian, A.; Bjornholm, T.; Vos, J. G.; Ulstrup, J. *Faraday Discuss.* **2006**, *131*, 265.
(28) Rotkina, L.; Lin, J. F.; Bird, J. P. *Appl. Phys. Lett.* **2003**, *83*, 4426–4428.
(29) Prokopuk, N.; Son, K. A.; Waltz, C. *J. Phys. Chem. C* **2007**, *111*, 6533–6537.
(30) Yamada, Y.; Sinsarp, A.; Sasaki, M.; Yamamoto, S. *Jpn. J. Appl. Phys.* **2003**, *42*, 4898–4900.
(31) Hahn, J. R.; Hong, Y. A.; Kang, H. *Appl. Phys. A: Mater. Sci. Process.* **1998**, *66*, S467–S472.
(32) Chen, P.; Gu, J.; Brandin, E.; Kim, Y. R.; Wang, Q.; Branton, D. *Nano Lett.* **2004**, *4*, 2293–2298.

DOI: 10.1021/nl103873a | *Nano Lett.* **2011,** *11,* 279–285